Depósito de investigación de la Universidad de Sevilla

https://idus.us.es/

Radiated power and soft X-ray diagnostics in the SMART Tokamak

J. Salas-Suárez-Bárcena,[1, a] L. F. Delgado-Aparicio,[2] J. Segado-Fernandez,[3] A. Rodriguez-Gonzalez,[1] K. A. McKay,[1] D. J. Cruz-Zabala,[1] J. Hidalgo-Salaverri,[3] J. Garcia-Dominguez,[2] M. Garcia-Muñoz,[1] E. Viezzer,[1] and J. Galdon-Quiroga[1]

[1)]Dept. of Atomic, Molecular and Nuclear Physics, University of Seville, Seville, 41012, Spain
[2)]Princeton Plasma Physics Laboratory, Princeton, New Jersey, NJ 08543, USA
[3)]Dept. of Mechanical Engineering and Manufacturing, University of Seville, Seville, 41092, Spain

(Dated: August 20, 2024)

A Multi-Energy Soft-X-Ray (ME SXR) diagnostic is planned to operate in the SMall Aspect Ratio Tokamak (SMART), consisting of five cameras: one for core measurements, two for edge, and two for divertors. Each camera is equipped with four Absolute Extreme Ultra-Violet (AXUV) diodes, with three of them filtered by Ti and Al foils for C and O line emissions respectively and Be foils for temperature measurements. Additionally, two spectrometers will be installed with a vertical line of sight for impurity control. This study introduces a synthetic model designed to characterize radiated power and soft X-ray (SXR) emissions. The developed code extracts radiated power and Z_{eff} values by leveraging distributions of electron density, temperatures, and impurity concentrations. The investigation is centered on the predicted scenarios of SMART's first phase of operation (I_p=100 kA; B_t=0.1 T), employing a double-null configuration with positive and negative triangularity. The anticipated impurities encompass C (1%) and Fe (0.01%) from the vessel, as well as O and N (0.1%) from air and water. For simplicity, the distribution is assumed to be homogeneous within the plasma, considering different mixtures with Z_{eff} values ranging between 1-2. Lastly, the model estimates signal strength for the diagnostic design proving its feasibility.

I. INTRODUCTION

In fusion reactors, power balance is a critical factor for feasibility, with radiative cooling being a significant source of power loss. Monitoring emissivity is crucial for achieving desired conditions during a plasma shot, as it provides valuable information on electron temperature (T_e) and density (n_e), and impurity concentrations (C_i)[1,2]. Radiated power (P_{rad}) in plasma primarily originates from three processes: Bremsstrahlung radiation, electron-ion recombination, and line emission from atomic electron de-excitation[3]. Absolute Extreme Ultra-Violet (AXUV) photodiodes, which are sensitive to soft X-rays (SXR) in the energy range of 3 to 3000 eV—a region in which most tokamaks emit—offer excellent signal-to-noise ratios and a fast time response of 0.5 μs. A Multi-Energy SXR (ME-SXR) diagnostic is capable of measuring all these variables. To achieve this, either digital or physical filters are used to narrow the spectral range. First, line-integrated radiated power is obtained directly from the signal of the detectors. Then, by isolating the detection through filtering to only Bremsstrahlung and recombination, electron temperature can be measured as $dP/dE \propto \exp(-E/T_e)$. Impurity concentrations are measured from line emissions, which are also well documented[4].

This type of diagnostic has already been successfully installed and operated in various magnetically confined plasma machines, including NSTX[5], WEST[6], and EAST[7]. A new ME-SXR diagnostic is planned for installation in the Small Aspect Ratio Tokamak (SMART), which is currently being commissioned by the Plasma Science and Fusion Technology (PSFT) team at the University of Seville. The concept of SMART's ME-SXR is similar to that of NSTX[5], utilizing physical filters and AXUV diodes with their signal later amplified. The diagnostic also employs two spectrometers for impurity control.

In this paper, an overview of the first operational phases of the SMART tokamak is provided, and the scenarios that this work is based on are presented (Section II). In Section III, we introduce and describe the design of this diagnostic. Subsequently, we discuss a model for radiated and SXR power specific to the SMART tokamak, along with the results. Finally, we estimate the signal strength for the different cameras of the SXR diagnostic (Section IV).

II. THE SMART TOKAMAK

SMART falls in the category of spherical tokamak as its aspect ratio is around 1.5. The objectives of this machine are: to study negative and positive triangularity plasmas, develop novel diagnostic techniques and exhaust alternatives, and to train the future generation of Fusion physicists and engineers[8,9,10].

SMART target plasma has a major radius of 0.5 m and minor radius of 0.25 with an elongation of around 2, giving a total volume of 1 m^3 . There are three operational phases planned for SMART (Table I), NBI will only be available after phase 2.

In this study, two different simulated plasma equilibria are analyzed using input data from the first operational phase of SMART. The magnetic equilibrium solver FIESTA[11] is employed to derive a distribution for the poloidal flux surfaces. By interpolating these results with the density and temperature outputs from the transport code ASTRA[12], the poloidal distributions of plasma density and temperature are obtained[10]. The scenarios considered include two double-null equilibria

a)Electronic mail: jsalas@us.es

Phase	1	2	3
I_p(kA)	100	500	>500
B_t(T)	0.1	0.4	1.0
τ_{pulse}(ms)	150	500	>1000
P_{ECRH}(kW)	6	6	200
P_{NBI}(kW)	-	400	1000

Table I: Operational phases for SMART. The electron cyclotron resonance heating (ECRH) for the first two phases will serve to preionize the plasma all the heating will be ohmic. In later phases a proper ECRH heating system will be installed

with positive and negative triangularities (Figure 1). A constant background density and temperature of 10^{15} m^{-3} and 0.01 eV, respectively, are assumed. It is important to note that these equilibria do not account for divertor or edge physics, so the derived values in these regions may vary.
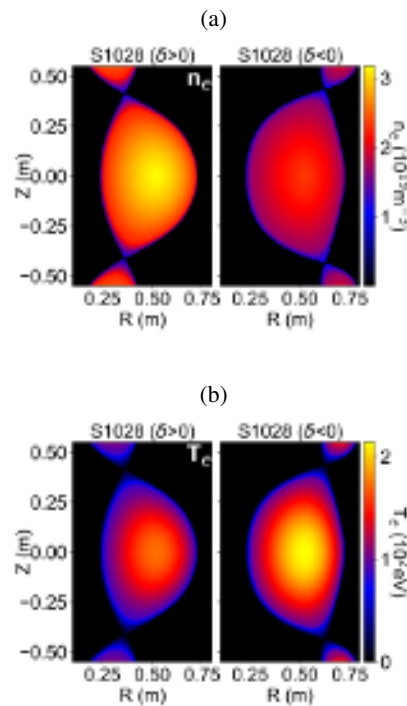

Figure 1: Electron density (1a) and electron temperature (1b) distributions from FIESTA and ASTRA simulations for positive (left) and negative (right) triangularity in SMART.

III. MULTI-ENERGY SOFT-X-RAY DIAGNOSTIC DESIGN

The ME-SXR diagnostic is planned to operate from the first phase of SMART, aiming to measure integrated radiated power, electron temperature and density, and impurity concentrations at five different regions. Figure 2a presents a 3D CAD model of the diagnostic, which consists of 5 groups of 4 pinhole cameras, each sharing the same view. Cameras U0 and L0 are aimed at the divertor, while the central camera C0 measures core radiation. The cameras CP and CN detect

emissivity closer to the edge. Additionally, two OceanOptics® spectrometers will provide measurements covering the spectral range from 185 to 1100 nm. Two optical fibers will collect light over vertical views on both the high field side and low field side of the plasma. Impurities are monitored by measuring the radiation levels at the peaks in the spectra associated with their line emissions.

As mentioned in Section I the design is similar to NSTX ME-SXR[5] but instead of an array of diodes per pinhole, only a single diode is used. All cameras share the same design, with a 5 mm diameter pinhole and diode and a distance between them of 60 mm. The resulting field of view FOV is of 9.5deg. Filters are allocated at the pinhole and are manually changeable to measure different regions of the spectra and line-emissions of different impurity species. For SMART first phase, each camera module (Figure 2b) has a specific purpose for each pinhole. One of them is completely uncovered to act as a bolometric reference. Two others are equipped with Be filters of 10 and 20 μm at the pinholes, allowing the measurement of Bremsstrahlung and recombination emissions (Figure 3) from which to extract T_e as mentioned in section I. The remaining pinhole, in the case of the C0 camera, is filtered by Ti 0.4 μm, which has a transmittance window matching the line emissions of C, thus providing information about the core radiation. For the rest of the cameras, Al filters of 0.4 μm will be used, targeting the measurement of O at the edges and in the divertor.

AXUV photodiodes are used to detect incoming radiation, providing good SNR and fast response (up to 0.5 μs). The signal amplification for each diode will vary: all pinholes in the C0 camera will employ variable gain low-noise transimpedance amplifiers with a bandwidth of up to 500 MHz from FEMTO®. The rest of the cameras will use fixed gain Thorlabs® amplifiers with a gain of 1 kV/A for the unfiltered pinhole and switchable gain of 1, 10, and 100 kV/A for the filtered ones. A National Instruments® data acquisition system will be employed to digitize the signals at a rate of 1 MHz.

IV. RADIATED POWER AND SXR EMISSIVITY IN SMART

A code to calculate radiated power was developed for this study. It consists of three blocks: plasma emissivity, detector constructor and signal generator. The first block uses poloidal distributions of electron density (n_e), electron temperature (T_e) and impurity concentrations (C_i). The ionization at any point in the plasma is considered in equilibrium with their surroundings (coronal equilibrium)[13], so the ionization distribution ($Z_i = Z_i(T_e)$) and cooling rates ($L_i = L_i(T_e)$) (Figure 4) can be described solely as a function of T_e. Then, applying charge neutrality as in Equation 1, the main specie's density is obtained. Each species contribution is summed through Equation 3.

$$n_e = \sum_i Z_i n_i = \sum_i Z_i C_i n_e \quad (1)$$

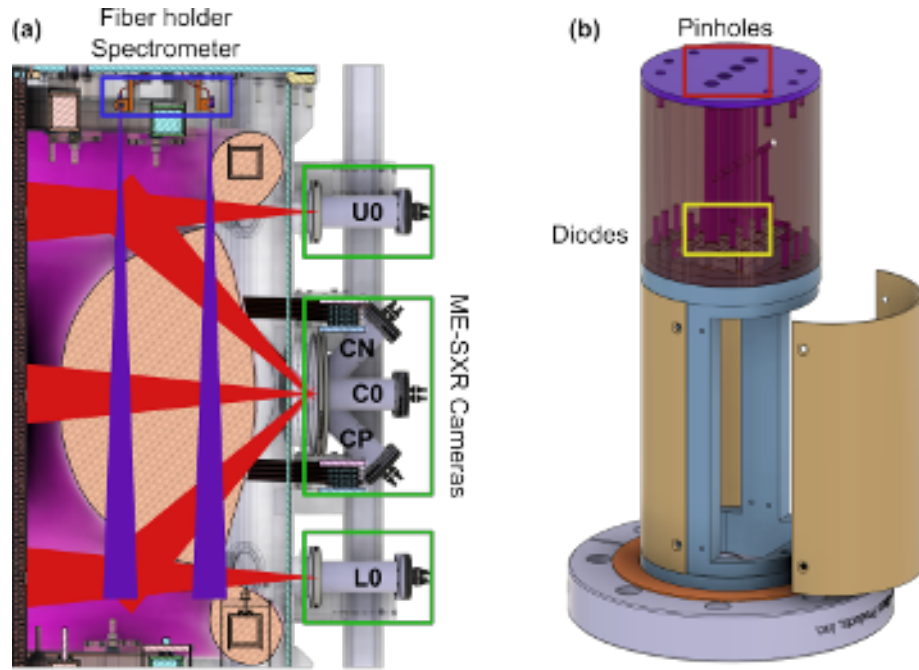With this result, it is possible to obtain the effective average

Figure 2: 3D model for SMART's ME-SXR diagnostic (a) and zoom of camera module (b). Each diode is connected with its own pinhole only except for a venting tube to prevent any pressure that can damage the filters. The connection to the vacuum feed-through is made with Kapton insulated coaxial cables encased in steel to reduce noise.
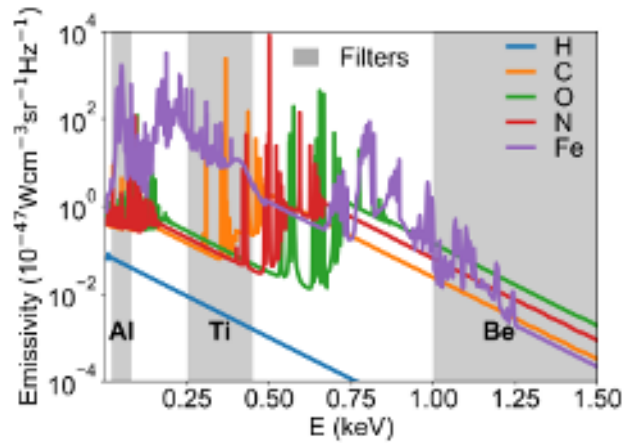

Figure 3: Spectral emissivity at 114 eV. The grey region indicates the target measurement region for each filter: both Be filters measure similar regions above 1 keV, the Ti filter's region of interest is between 250 and 450 eV, and the Al filter targets between 20 and 80 eV.

charge (Z_{eff}) and P_{rad}, using (2) and (3).

$$Z_{eff} = \frac{\sum_i Z_i^2 n_i}{\sum_i Z_i n_i} = \sum_i Z_i^2 C_i \qquad (2)$$

$$P_{rad} = \sum_i L_i n_i n_e = \sum_i L_i C_i n_e^2 \qquad (3)$$

Using FLYCHK, an atomic level population distribution solver for plasmas[14], it is possible to expand the study for spectral emissivity summing each species contribution (see

Equation 3). Resulting, in obtaining the power radiated in the SXR region (P_{SXR}).

Mixes		1	2	3	4
C_i (%)	C	0.00	1.00	2.00	3.00
	O	0.00	0.10	0.10	0.50
	N	0.00	0.10	0.10	0.50
	Fe	0.00	0.01	0.01	0.01
$< Z_{eff} >$		1.00	1.29	1.52	1.97
$P_{rad}(Total)$ (kW)		0.12	20.52	24.42	34.72

Table II: Cases of impurities for SMART S1028 equilibria from FIESTA and ASTRA codes. The total radiated is defined as the integral over the whole plasma.

The plasmas considered for this study were hydrogenic, with four evaluated impurities: C from graphite used for limiters, Fe from the steel vessel, O from water condensed inside the vessel, and N from air. As shown in Figure 4, most of the plasma in these equilibria is at temperatures where C peaks in emissivity. Additionally, Fe emits 4 orders of magnitude more than the other species. High radiative power is expected as both the vessel and divertor coil casings are made of steel.

Considering other steel wall machines with carbon tiles, such as ADITYA[15] and TJ-II[16], the effective charge number (Z_{eff}) for densities and temperatures similar to those anticipated in the first phase of SMART's operation is approximately 2. To estimate Z_{eff} values ranging from 1 (pure hydrogen) to 2, four different impurity mixtures were analyzed, utilizing values analogous to those in the aforementioned machines (see Table II). Given that SMART will be equipped with a baking system operating at 180 ºC, low concentrations of N and O are expected. Nonetheless, as depicted in Table II and Figure 5, even small concentrations of impurities lead
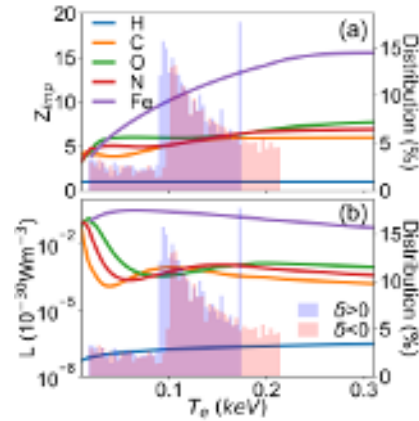
This approximation, however, is not valid for SMART ME-SXR. In this case, the volumetric integral is computed by integrating over a cone-shaped array of points, or mesh, which is generated by the second block based on specific geometric parameters. This mesh represents the points whose emitted light will reach the detector through the pinhole. The cone angle for generating the mesh is determined by the distance between the detector and the pinhole, their sizes, and their relative orientation. Finally, the third block evaluates the emissivity of this mesh and, utilizing the responsivity of the diodes along with the characteristics of the pinhole filters, calculates the signal strength.

Figure 4: Average ion charge (a) and Cooling rates (b) for H, C, O, N and Fe, compared to the temperature distribution of S1028 simulation in positive and negative triangularity.

Figure 6: SMART's ME-SXR filters transmittances and responsivity of AXUV photidodes[18]. The filters of Al and Ti have a window of transmittance that allows for line-emissions of C and O respectively. All filters tend to 100% transmittance in the Bremsstrahlung region where the emissivity is proportional to $\exp(-E/T_e)$.

to a significant increase in radiative power, by approximately two orders of magnitude. C and Fe are predicted to be the predominant contributors to this level of emission. In terms of soft X-ray (SXR) emissivity, only 1% of the total radiated power is emitted within this regime (Figure 5c and d).
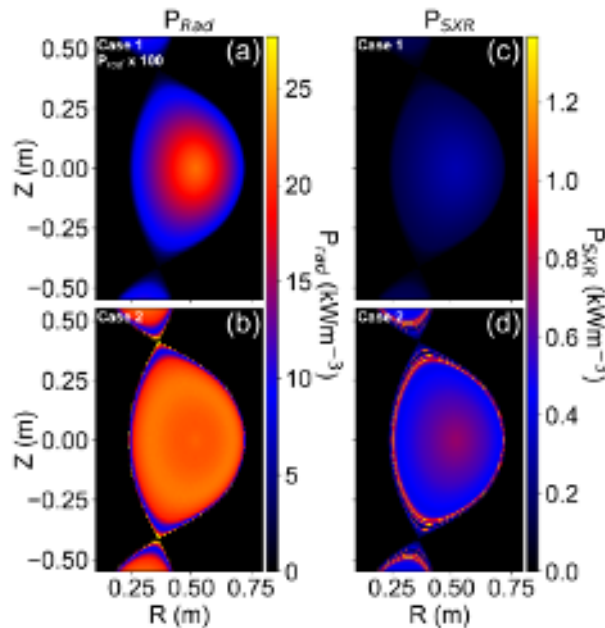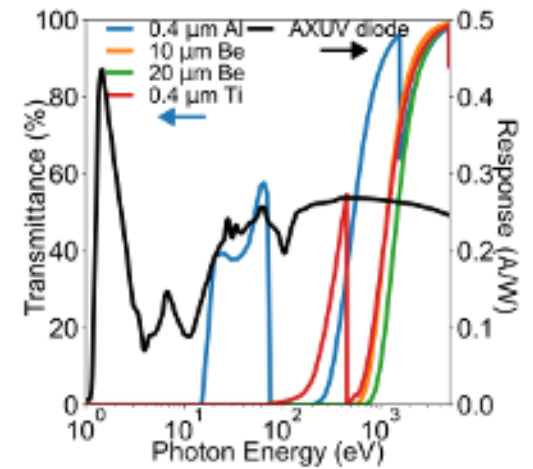

Figure 5: Radiated power (P_{rad}) for positive triangularity equilibrium for case 1 times 100 (a) and case 2 (b). Soft X-ray power (P_{SXR}) for case 1 (c) and 2 (d).

The radiated power reaching the detector is a volumetric integral over the region where light can pass through the pinhole to the detector. For a sufficiently narrow FOV, this can be approximated as the product of the line-integrated radiated power and the etendue (η), as shown in Equation 4[17].

$$P_{det} = \int_{V_{det}} d\mathbf{r} \frac{\Omega_{det}}{4\pi} P_{rad}(\mathbf{r}) \approx \frac{\eta}{4\pi} \int_{l_{det}} ds P_{rad}(\mathbf{r}) \quad (4)$$

SMART's ME-SXR system, as discussed in Section III, can be used as input for the computational model. AXUV diodes (Figure 6) exhibit an average responsivity of 0.25 A/W, although they are not sensitive to low-energy regions. Considering the filters employed, a substantial decrease in the radiated power reaching the diodes is expected.

In Figure 7, the coverage area for each camera is depicted. In this specific positive triangularity equilibrium, the plasma shape is expected to vary. Using the computational model, the anticipated signals for the cameras are projected to have currents on the order of milliamps (mA) for the unfiltered pinholes of the central cameras. The signals decrease to microamps (μA) for the filtered pinholes in the central cameras and for the unfiltered pinholes at the divertor cameras. The lowest signals, in the range of nanoamps (nA), are observed for the filtered pinholes at the divertor cameras. Given that the data acquisition system can handle a maximum signal of ±10 V, the amplification provided by SMART's ME-SXR system should be adequate to capture the signal without saturation.

Regarding noise levels, the photodiode requires a constant voltage for operation, resulting in the generation of a small current, known as dark current, approximately 100 nA for AXUV diodes. Consequently, divertor signals may become undetectable. However, as discussed in Section II, the model
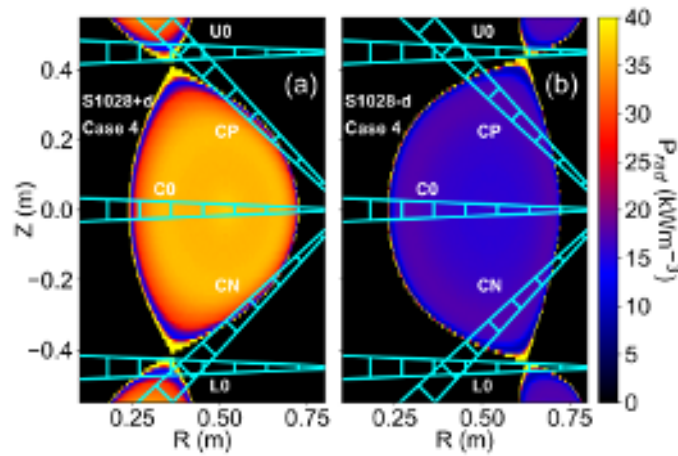
Figure 7: ME-SXR cameras in P_{rad} poloidal distributions in positive (a) and negative (b) triangularity.

does not produce realistic density and temperature values in these regions. Furthermore, this study focuses solely on the initial phase of SMART, potentially leading to higher signal levels.

Overall, all channels will receive sufficient light to produce a big enough signal even with a small FOV. Still, the pinholes sizes for the camera modules can be changed allowing more or less light to go through.

V. CONCLUSIONS

For SMART first operational campaign a ME-SXR diagnostic is planned to be installed and its design has been finalized. AXUV photodiodes have been chosen for light collection, due to their sensitivity to ultraviolet and SXR. Be, Al and Ti filters have been chosen for studying electron density and temperature, radiated power and impurity concentrations. Two spectrometers were chosen to complement for impurity control.

A code has been developed to estimate the radiated power and spectral emissivity for SMART's first operational phase. Different cases of impurities were evaluated with Z_{eff} between 1 and 2, increasing the radiated power a hundred fold with small impurity concentrations. Finally, signal strengths ranging from mA to nA have been predicted for SMART's ME-SXR diagnostic which matches the selected gains for the amplifiers. The SNR was evaluated granting signals under 100 nA lost. Although this affects more cameras U0 and L0 cameras the signal may be underestimated due to codes computing edge and divertor physics.

VI. ACKNOWLEDGMENTS

VII. DATA AVAILABILITY

The data upon which this article is based is freely available upon request under reasonable terms.

REFERENCES

[1]D. J. Clayton, K. Tritz, D. Stutman, M. Finkenthal, S. M. Kaye, D. Kumar, B. P. LeBlanc, S. Paul, and S. A. Sabbagh, Plasma Physics and Controlled Fusion **54**, 105022 (2012).

[2]L. F. Delgado-Aparicio, J. Maddox, N. Pablant, K. Hill, M. Bitter, J. E. Rice, R. Granetz, A. Hubbard, J. Irby, M. Greenwald, E. Marmar, K. Tritz, D. Stutman, B. Stratton, and P. Efthimion, Review of Scientific Instruments **87**, 11E204 (2016), https://pubs.aip.org/aip/rsi/article-pdf/doi/10.1063/1.4964807/16053260/11e204_1_online.pdf.

[3]I. H. Hutchinson, *Principles of Plasma Diagnostics*, 2nd ed. (Cambridge University Press, 2002).

[4]L. Delgado-Aparicio, *Novel soft x-ray diagnostic techniques for the study of particle transport phenomena in magnetically confined fusion plasmas* (2008).

[5]K. Tritz, D. J. Clayton, D. Stutman, and M. Finkenthal, Review of Scientific Instruments **83**, 10E109 (2012), https://pubs.aip.org/aip/rsi/article-pdf/doi/10.1063/1.4731741/13703458/10e109_1_online.pdf.

[6]O. Chellai, L. F. Delgado-Aparicio, P. VanMeter, T. Barbui, J. Wallace, K. W. Hill, N. Pablant, B. Stratton, C. Disch, B. Luethi, and N. Pilet, Review of Scientific Instruments **92**, 043509 (2021), https://pubs.aip.org/aip/rsi/article-pdf/doi/10.1063/5.0043456/14029810/043509_1_online.pdf.

[7]Y. L. Li, G. S. Xu, K. Tritz, Y. B. Zhu, B. N. Wan, H. Lan, Y. L. Liu, J. Wei, W. Zhang, G. H. Hu, H. Q. Wang, Y. M. Duan, J. L. Zhao, L. Wang, S. C. Liu, Y. Ye, J. Li, X. Lin, and X. L. Li, Review of Scientific Instruments **86**, 123512 (2015), https://pubs.aip.org/aip/rsi/article-pdf/doi/10.1063/1.4938155/15839753/123512_1_online.pdf.

[8]S. J. Doyle, D. Lopez-Aires, A. Mancini, M. Agredano-Torres, J. L. Garcia-Sanchez, J. Segado-Fernandez, J. Ayllon-Guerola, M. Garcia-Muñoz, E. Viezzer, C. Soria-Hoyo, J. Garcia-Lopez, G. Cunningham, P. F. Buxton, M. P. Gryaznevich, Y. S. Hwang, and K. J. Chung, Fusion Engineering and Design **171**, 112706 (2021).

[9]A. Mancini, J. Ayllon-Guerola, S. J. Doyle, M. Agredano-Torres, D. Lopez-Aires, J. Toledo-Garrido, E. Viezzer, M. Garcia-Muñoz, P. F. Buxton, K. J. Chung, J. Garcia-Dominguez, J. Garcia-Lopez, M. P. Gryaznevich, J. Hidalgo-Salaverri, Y. S. Hwang, J. Segado-Fernández, and the PSFT team, Fusion Engineering and Design **171**, 112542 (2021).

[10]A. Mancini, L. Velarde, E. Viezzer, D. J. Cruz-Zabala, J. F. Rivero-Rodriguez, M. Garcia-Muñoz, L. Sanchis, A. Snicker, J. Segado-Fernandez, J. Garcia-Dominguez, J. Hidalgo-Salaverri, P. Cano-Megias, M. Toscano-Jimenez, and the PSFT team, Fusion Engineering and Design **192**, 113833 (2023).

[11]G. Cunningham, Fusion Engineering and Design **88**, 3238 (2013).

[12]G. V. Pereverzev and P. N. Yushmanov, (2002).

[13]R. A. Hulse, Nuclear Technology - Fusion **3**, 259 (1983), https://doi.org/10.13182/FST83-A20849.

[14]H. K. Chung, M. H. Chen, W. Morgan, Y. Ralchenko, and R. W. Lee, High Energy Density Physics **1**, 3 (2005).

[15]M. B. Chowdhuri, R. Manchanda, J. Ghosh, K. A. Jadeja, K. M. Patel, V. Kumar, K. M. Patel, P. K. Atrey, Y. S. Joisa, S. B. Bhatt, R. L. Tanna, and A. team, Plasma Physics and Controlled Fusion **62**, 035015 (2020).

[16]B. Zurro, E. M. Hollmann, A. Baciero, M. A. Ochando, K. J. McCarthy, F. Medina, J. L. Velasco, I. Pastor, D. Baião, E. de la Cal, D. Rapisarda, and the TJ-II Team, Plasma Physics and Controlled Fusion **56**, 124007 (2014).

[17]M. Anton, H. Weisen, M. J. Dutch, W. W von der Linden, F. Buhlmann, R. Chavan, B. Marletaz, P. Marmillod, and P. Paris, Plasma Physics and Controlled Fusion **38**, 1849 (1996).

[18]M. Bernert, T. Eich, A. Burckhart, J. C. Fuchs, L. Giannone, A. Kallenbach, R. M. McDermott, B. Sieglin, and A. U. Team, Review of Scientific Instruments **85**, 033503 (2014), https://pubs.aip.org/aip/rsi/article-pdf/doi/10.1063/1.4867662/15602110/033503_1_online.pdf.